

Failure Behavior of Electroplated Co₆₀Ru₄₀ layer on NiSi_x/Si Substrate for Copper Metallization

Jiun Yi Tseng, Wen Jauh Chen*, and Kuan Chen Wu

Graduate School of Materials Science, National Yunlin University of Science and Technology, 123 University Road, Section 3, Douliou, Yunlin 64002, Taiwan.

*E-mail: chenwjau@yuntech.edu.tw

Received: 2 August 2021 / Accepted: 7 September 2021 / Published: 10 October 2021

To avoid copper diffusion into silicon substrates and prevent the formation of copper silicide, a thin layer (diffusion barrier) between the copper layer and silicon substrate is introduced. A thin cobalt-ruthenium barrier layer and copper were deposited on textured (001) silicon with nickel silicide by an electroplating method in this work. The sample presents Cu/Co₆₀Ru₄₀/NiSi_x/Si. The structures of Cu/Co₆₀Ru₄₀/NiSi_x/Si were characterized by scanning transmission electron microscopy (SEM), scanning electron microscopy (STEM), energy dispersive X-ray spectrometry (EDS), and powder X-ray diffraction (XRD). The results show that cobalt atoms diffuse more easily to nickel silicide than ruthenium atoms at high temperatures. The failure of Cu/Co₆₀Ru₄₀/NiSi_x/Si can be attributed to copper penetration through the Co₆₀Ru₄₀ and nickel silicide layers and the formation of copper silicide.

Keywords: Textured silicon; Electroplating; Solar cells; Diffusion barrier

1. INTRODUCTION

Solar cell development has occurred over more than 40 years. In recent years, the proportion of solar cell power generation has increased annually. The global crystalline silicon cell and PV module production capacity at the end of 2020 is estimated to be approximately 300 GWp, according to the 2021 International Technology Roadmap for Photovoltaic (ITRPV) report [1]. To ensure the long-term competitiveness of solar cell power generation. It is necessary to reduce manufacturing costs and improve the performance of cells and modules to support the reduction of solar cell costs. In crystalline silicon solar cells, the formation of metal contacts affects component efficiency and long-term reliability. Additionally, the building of metal contacts is one of the critical steps in crystalline silicon solar cell manufacturing.

In the front side metallization of silicon solar cells, screen-printed silver paste has been widely used to form metal contacts on commercial solar cells due to its low resistance, smooth operation, and suitable mass production. However, screen printing still has several significant disadvantages, including paste containing glass frits, high costs, high-temperature firing, and shadowing [2-5]. Many front-side metallization technologies have been developed to overcome the drawbacks of screen printing. Among them, copper metallization has the advantages of low cost and high conductivity and is one of the most promising candidates to replace screen printing. In addition, the use of electroplating copper instead of silver achieves higher solar cell efficiency.

Applying electroplating copper technology to the front metallization of solar cells can overcome the shortcomings of screen printing. However, copper has a high diffusion coefficient and high solubility in silicon (even at room temperature, it will spread to the silicon substrate, forming copper silicon compounds). Copper-contaminated solar cells will reduce the performance of solar cells due to the introduction of minority carrier recombination centers [6-8]. To avoid copper diffusion into the silicon substrate and prevent the formation of copper silicide. A thin layer between the copper and silicon substrates is introduced thus avoiding direct contact between copper and the bottom Si. This thin layer is the so-called diffusion barrier layer. In microelectronics, many potential diffusion barriers have been developed thus far. The most widely used materials for the diffusion barrier are TiN, TaN, ITO, WN, TiW, Ru, Ru-Ta-C, Ru(P), and Ti-Ta-N [9-17]. Barrier materials are typically applied by sputtering or physical vapor deposition (PVD) [9-17]. In addition, a flat and polished silicon substrate is used in microelectronics. For a single crystal silicon solar cell, the surface of silicon is textured and unpolished. Therefore, the diffusion barrier properties applied to silicon solar cells may be different from those of flat and polished silicon substrates. Additionally, vacuum processes are more expansive than electroplating. The barrier materials have reliable Cu diffusion barrier properties during thermal degradation and prevent corrosion of electrolytes of electroplating copper [18]. To date, there has been little work regarding the diffusion barrier in solar cells when copper metallization is introduced to solar cell manufacturing [19-22].

Recently, Huang et al. reported the effect of thermal stress on copper electroplated crystalline silicon solar cells [19, 20]. Huang et al. prepared solar cells using CMOS (complementary metal-oxide-semiconductor) grade and without textured (100) silicon as a substrate. Their report confirmed that solar cell degradation at 150 °C was closely related to Cu diffusion. They also found that only the Ni₂Si layer cannot prevent copper diffusion into silicon at 200 °C. The presence of the Ni layer on Ni₂Si delays copper diffusion into silicon at 200 °C. The cell performance deterioration with a thin nickel layer is more severe than that with a thick nickel layer.

Additionally, the authors also found that the Ni₇₁Co₂₉ alloy layer significantly delayed cell degradation at 250 °C [19]. The delay of cell degradation can be attributed to decreased silicidation of the NiCo alloy [20]. Our previous study also found that copper diffused into silicon and formed Cu₃Si after annealing at 300 °C for 10 min in the Cu/Ni (60 nm)/NiSi/Si system [21]. Therefore, using a diffusion barrier layer other than nickel is one of the critical issues to improve the long-term stability of solar cells in copper metallization. To act as excellent diffusion barriers, copper must have excellent bonding properties, low resistivity, and limited solubility. Pure cobalt, pure ruthenium, or ruthenium-cobalt alloys are notable examples [22, 23]. We also reported that the Cu/Ru_yCo_{1-y}/NiSi_y/Si stack with

the $y = 0.9-0.6$ sample could be maintained up to 400 °C [23]. Few studies have focused on the failure behavior of electroplating cobalt-ruthenium alloy layers on textured silicon for solar cells. This study explored the failure mechanism of electroplating cobalt-ruthenium alloy ($\text{Co}_{60}\text{Ru}_{40}$).

2. EXPERIMENTAL

Single crystal, phosphorus-doped, pyramid-textured, silicon wafers were used as substrates. The cleaning process of the textured silicon substrate surface was as follows: First, the substrate was degreased in acetone by ultrasonication, and a $\text{H}_2\text{SO}_4/\text{H}_2\text{O}_2$ solution was used to remove metal ions and form silicon oxide. Then, the substrate was dipped into hydrogen fluoride solution to remove native oxide to obtain the fresh surface of textured silicon. The nickel film was deposited on the clean surface of textured silicon by an electroless plating method. Silicon is a semiconductor and it is difficult to deposit a metal film on silicon without pretreatment by an electroless plating method. The pretreatment of silicon included sensitization and activation. A solution of sensitization comprised SnCl_2 and HCl , and an activation solution consisted of PdCl_2 and HCl . After sensitization and activation, a metal film was formed onto textured silicon (electroless plating). In this study, the electroless plating method created a thin nickel film. The electroless bath had a temperature of 70 °C and a pH value of 5. The plating time was 60 seconds.

The as-deposited electroless nickel thin film substrate was first annealed in a furnace at 500 °C in an Ar/H_2 atmosphere for 10 minutes to form nickel silicides. Then, the HNO_3 solution was etched to remove the excess nickel metal to obtain the clean surface of the annealing sample, which was designed as NiSi_x/Si . The clean NiSi_x/Si substrate was used to further electroplate cobalt-ruthenium alloy and copper films. The substrate dimension was 20 mm × 20 mm. Electroplating cobalt-ruthenium alloy and copper on NiSi_x/Si substrates was conducted in chemical baths. Reagent-grade chemicals were dissolved in deionized water and formed chemical bath solutions. For the electroplating bath of cobalt-ruthenium alloy, the electrolyte was composed of $\text{RuCl}_3 \cdot \text{H}_2\text{O}$ (10 g/L), $\text{CoSO}_4 \cdot 7\text{H}_2\text{O}$ (50.2 g/L), and H_3NSO_3 (9.75 g/L). The copper electroplating bath was a commercial copper sulfate solution. An electroplating cell was a beaker of 300 mL. Magnetic stirrer agitation was applied during electroplating. The electroplating bath temperatures were 25 and 60 °C for copper and cobalt-ruthenium plating, respectively. For cobalt-ruthenium alloy and copper electrodeposition, a platinum plate was selected as the anode material. The size of a platinum plate was 20 mm × 20 mm. For cobalt-ruthenium plating, the electroplating current density was fixed at 20 mA/cm^2 , and the plating time was 40 seconds. For copper plating, the electroplating current density and time of the copper layer were 40 mA/cm^2 and 4 minutes, respectively. The electroplating cobalt-ruthenium and copper metals on NiSi_x/Si were designed as $\text{Cu}/\text{CoRu}/\text{NiSi}_x/\text{Si}$. Finally, the $\text{Cu}/\text{CoRu}/\text{NiSi}_x/\text{Si}$ samples were annealed at 300–800 °C for 10 min in Ar/H_2 ambient conditions.

A JEOL scanning electron microscopy (SEM) instrument operating at 20 kV was used for surface morphological examination. Scanning transmission electron microscopy (STEM) was performed with a JEM-ARM200F instrument. SEM with energy dispersive X-ray spectroscopy (EDS, Oxford Link) was used to determine the chemical composition of all samples. The STEM-EDS compositional maps

were also generated using an EDS detector (JEOL Ltd.) to collect X-rays. Powder X-ray diffraction (XRD) analyses were performed on a Bruker D8 Advance diffractometer with Cu K α radiation.

3. RESULTS AND DISCUSSION

Figure 1 (a) presents an SEM micrograph for the sample in which a cobalt-ruthenium alloy film was deposited onto the single-crystal silicon substrate with nickel silicide (CoRu/NiSi_x/Si). Many pyramid shapes can be observed on the surface of this substrate.

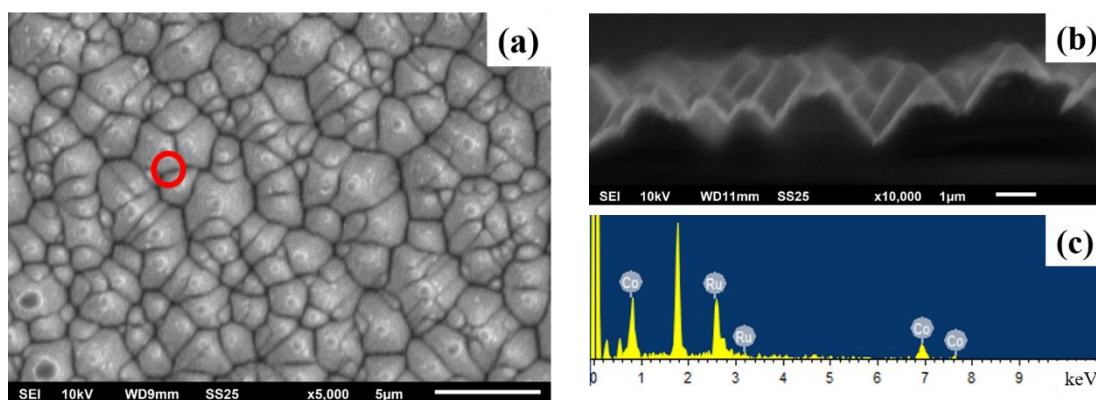


Figure 1. (a) SEM micrograph of the surface structure of the plated CoRu film. (b) SEM micrograph for the cross-sectional view of the plated CoRu sample. (c) EDS spectra of the CoRu sample.

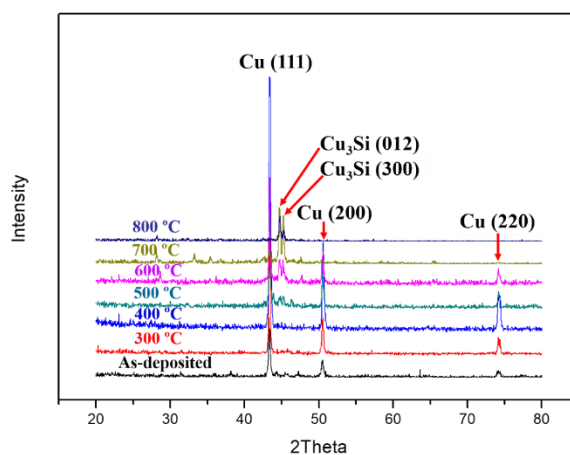
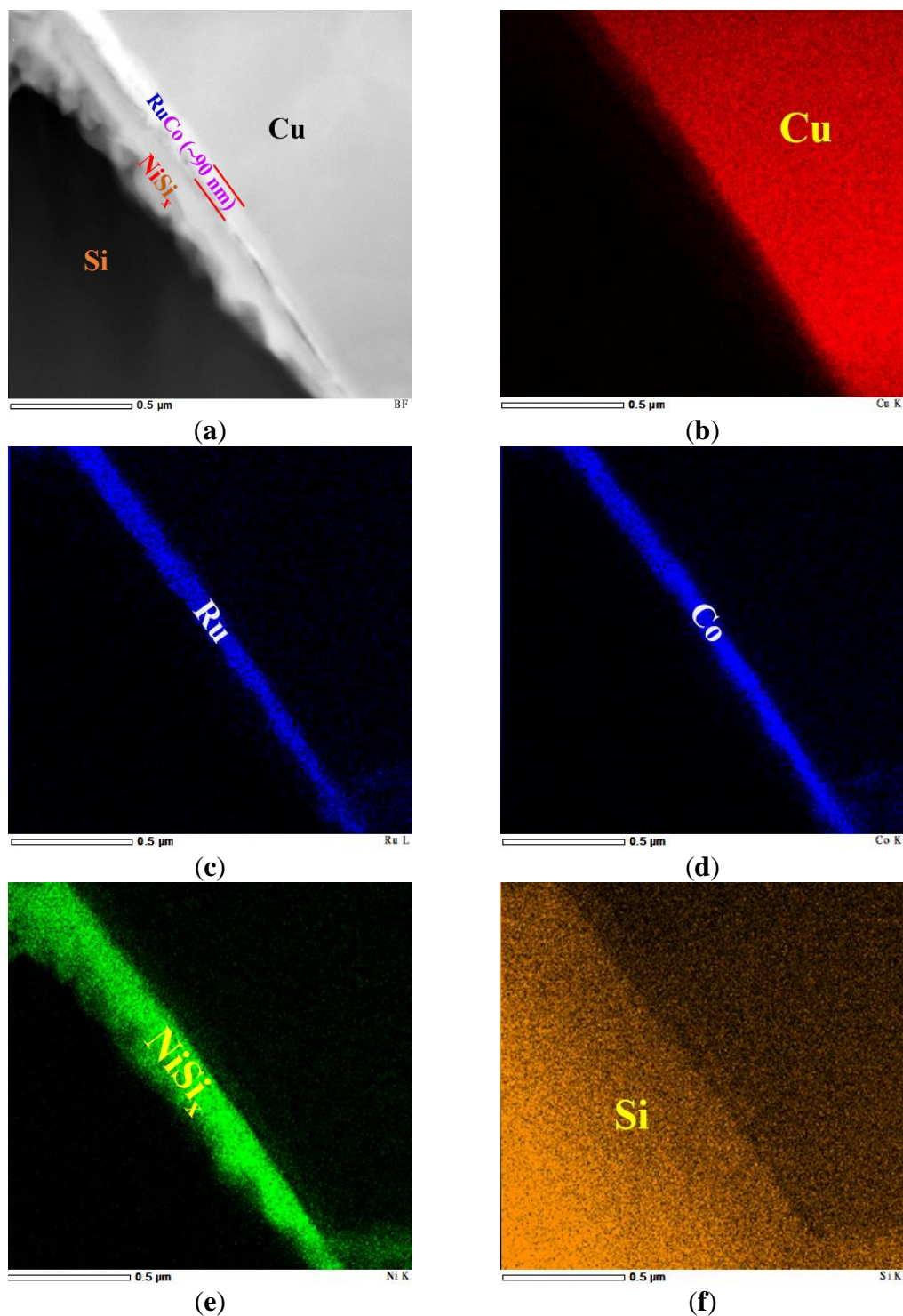


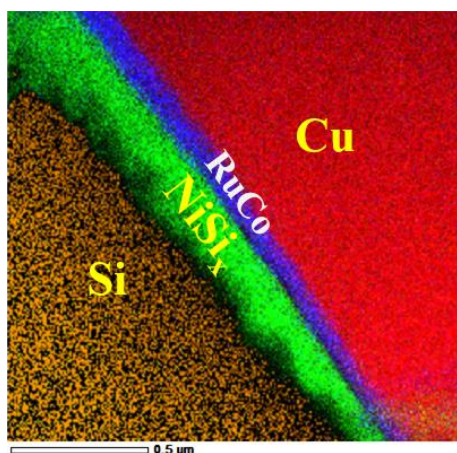
Figure 2. X-ray diffraction patterns of Cu/Co₆₀Ru₄₀/NiSi_x/Si samples annealed at various temperatures (300–800 °C) for 10 min.

It is a thin layer on the surface from a cross-sectional view of the SEM image (Figure 1 (b)). Figure 1 (c) shows the circle area composition analysis of the signals of ruthenium and cobalt elements from the SEM-EDS measurement. The atomic ratios of ruthenium and cobalt are approximately 40 and 60, respectively. That is, the composition of the CoRu alloy is Co₆₀Ru₄₀. The voltage, current, and time

of the electroplating process can influence the composition and thickness of CoRu alloy. The thickness of CoRu alloy increases as the current and time of electroplating increase.

XRD analyses were carried out to obtain information about the phase formation during annealing. XRD spectra for the as-deposited sample and samples annealed at 300–800 °C are presented in Fig. 2. The most energetic intensity of the diffraction peak could be indexed to Cu (111). The diffraction peaks belonging to copper can be seen clearly when the sample annealing temperature was below 600 °C.





(g)

Figure 3. (a) STEM image of the sample annealed at 300 °C, EDS map of (b) Cu, (c) Ru, (d) Co, (e) Ni, (f) Si, and (g) an overlay of Cu, Ni, Ru, Co, and Si EDS maps.

The intensities of the Cu_3Si (012) and (300) peaks presented at temperatures higher than 500 °C. Based on these XRD spectra, copper silicide formed when the annealing temperature was higher than 500 °C. Some weak diffraction peaks at 45–50 degrees can be identified, in which Ni_2Si and NiSi phases can be identified. Thus, we can conclude from the XRD spectra in Figure 2 that copper readily diffuses into silicon and forms copper silicide above 500 °C.

Figure 3 (a) is a STEM micrograph showing the layered structure of the $\text{Cu}/\text{Co}_{60}\text{Ru}_{40}/\text{NiSi}_x/\text{Si}$ sample annealed at 300 °C for 10 min in an Ar/H_2 environment. STEM-EDS can provide elemental maps as a powerful method to locate all layers. The EDS maps of Cu, Ru, Co, Ni, and Si are shown in Fig. 3 (b)-(f), respectively. EDS maps of Fig. 3 (b)-(f) use the Cu K, Ru L, Co K, Ni K, and Si K lines. Fig. 3 (g) shows an overlap of Cu, Ru, Co, Ni, and Si maps. The intensity of the red layer in Fig. 3(b) and (g) shows that it is composed of Cu without Ni, Ru, Co, and Si. Fig. 3 (c) and (d) are ruthenium and cobalt element maps, respectively. We can see that the Ru and Co layers have the same profile. Moreover, the Ru layer overlaps with the Co layer entirely from Figures (c) and (d). This result indicated that Ru and Co formed the CoRu alloy layer. Fig. 3 (e) shows the Ni spectra that can be easily identified as belonging to the chemical phases of Ni. Fig. 3 (f) belongs to Si. The nickel layer overlaps with part of the silicon layer from Figures (e) and (f), which reveals that the overlap area of Ni and Si is a nickel silicide layer.

STEM-EDS line scanning can be used to measure the profile of the element in the $\text{Cu}/\text{Co}_{60}\text{Ru}_{40}/\text{NiSi}_x/\text{Si}$ structure. The composition analysis was carried out across the multilayer stack using STEM-EDS, as shown in Figure 4. Fig. 4 (b) presents the atomic concentration of various element profiles in the rectangular area, which are shown in Figure 4 (a). The distribution of copper in the stack was found to concentrate on the copper layer. This finding suggested that copper did not diffuse into the silicon substrate. The signals of ruthenium and cobalt emerged at 0.5–0.6 μm intervals. The sign of elemental cobalt is higher than that of ruthenium, which reveals that the cobalt concentration was higher than that of ruthenium in the CoRu alloy layer. The thickness of CoRu was estimated to be smaller than 100 nm. The distribution of nickel was located at a scale between 0.3 and 0.52 μm . The NiSi_x layer was situated in the CoRu layer and Si structure.

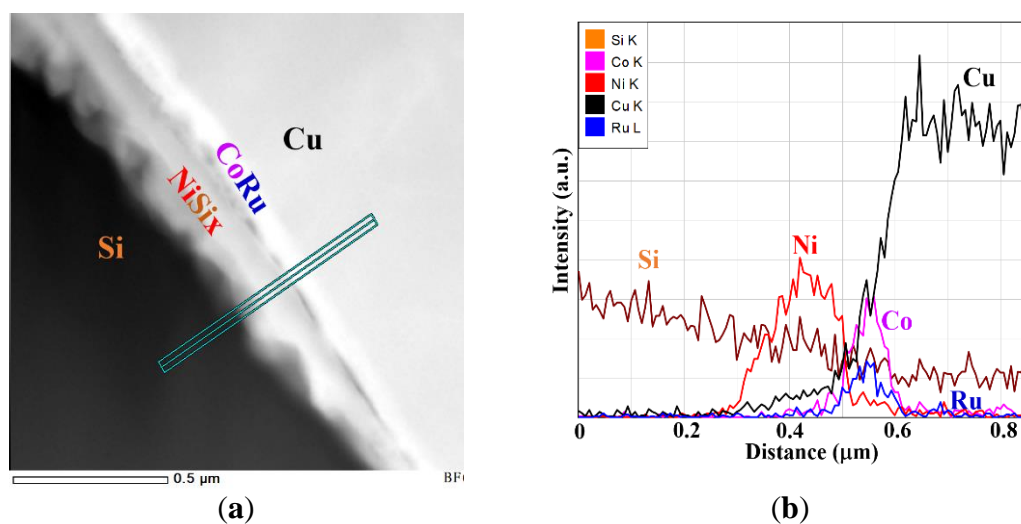
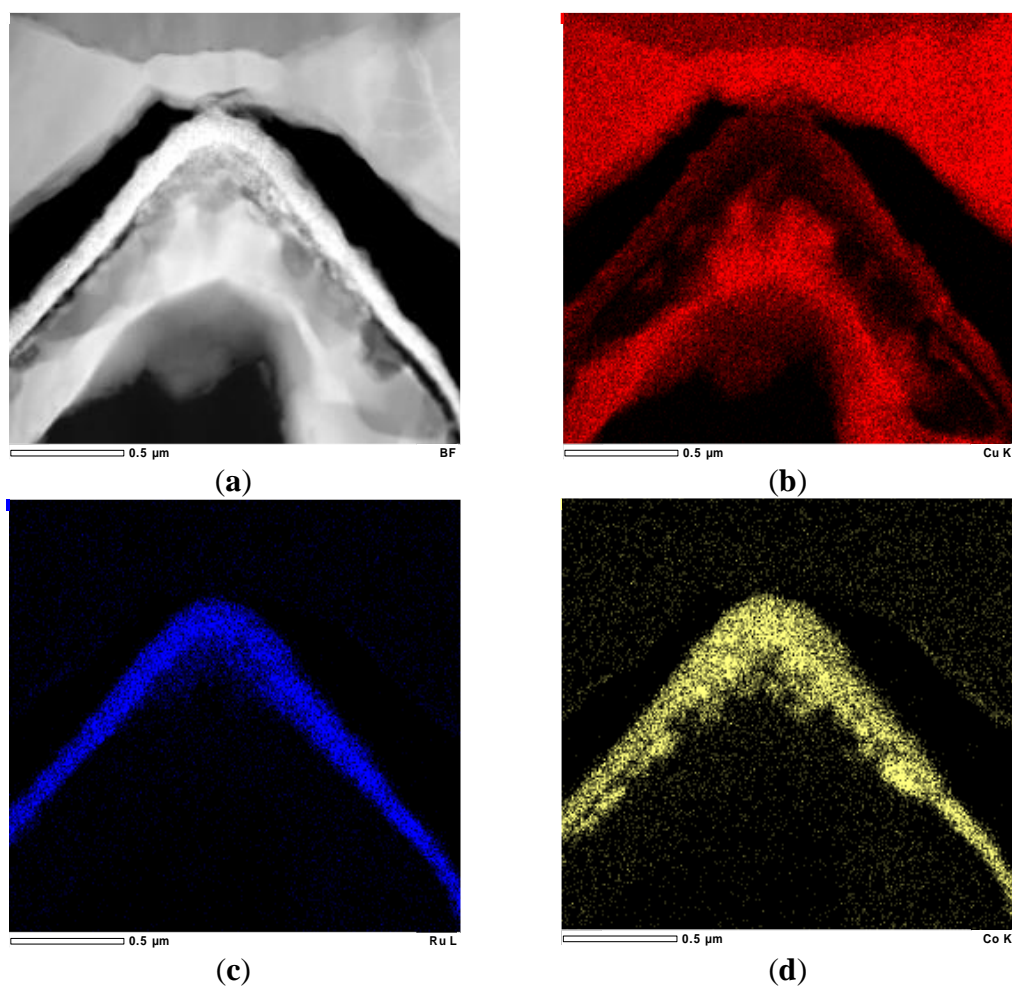


Figure 4. (a) STEM bright-field image of the sample annealed at 300 °C. (b) The composition analysis was carried out across the stack using STEM-EDS.



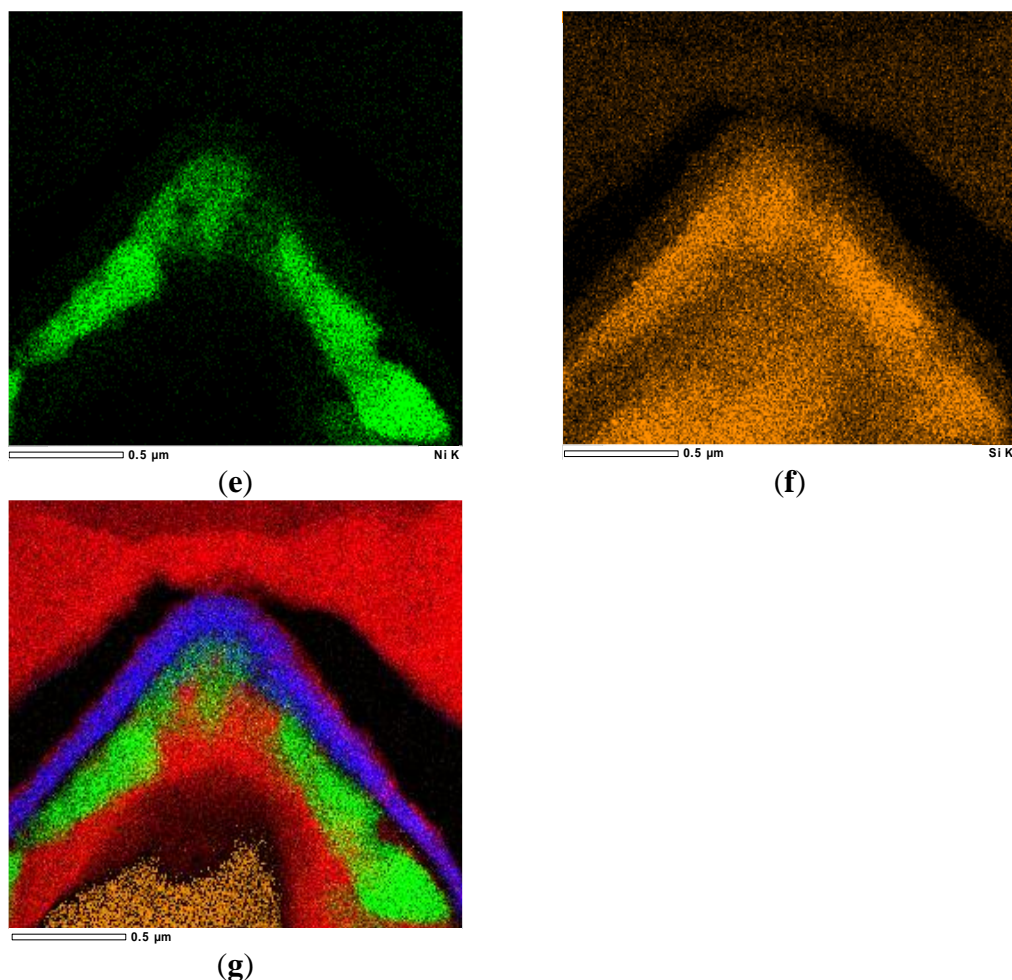


Figure 5. (a) STEM bright-field image of the sample annealed at 500 °C, EDS map of (b) Cu, (c) Ru, (d) Co, (e) Ni, (f) Si, and (g) an overlay of Cu, Ni, Ru, Co, and Si EDS maps.

A STEM bright-field micrograph of the Cu/Co₆₀Ru₄₀/NiSi_x/Si sample annealed at 500 °C is presented in Figure 5 (a). The CoRu alloy layer below the copper layer seems to be preserved after annealing at 500 °C for 10 min. However, there is a large gap between the CoRu and Cu layers. Fig. 5 (b)-(f) shows the EDS maps of Cu, Ru, Co, Ni, and Si, respectively. Fig. 5 (g) shows the overlap of Cu, Ru, Co, Ni, and Si maps. In Figure 5 (b) and (g), the elemental copper map reveals that Cu is present in all layers, showing that Cu atoms diffused from the Cu film through the CoRu layer and nickel silicides into silicon. Additionally, it reacted with silicon to form copper silicide in the silicon substrate. The copper silicide is the Cu₃Si phase, according to XRD spectra (Figure 2).

To understand the distribution of all elements in the Cu/Co₆₀Ru₄₀/NiSi_x/Si sample after annealing at 500 °C, the elemental profiles measured by STEM line scanning mode are shown in Figure 6. The elemental profile presented in Fig. 6 (b) scanned the rectangular area shown in Figure 6(a). The vigorous intensity of the copper signal in the Cu/Co₆₀Ru₄₀/NiSi_x/Si stack was found on the right side (1.2–1.4 μm) and at 0.48–0.8 μm intervals. The chemical compositions in Fig. 6 (c) and (d) are the red circles 1 and 2 (spots 1 and 2, respectively) shown in Figure 6 (a), respectively. Spot 1 is located in the CoRu thin layer. The atomic ratio of Co and Ru was ~5:5. The main elements are copper and silicon in spot two, which reveal the copper silicide formed in the silicon substrate. This finding suggested that many copper atoms diffused into the silicon substrate. We can also observe that strong intensities of the Cu signal are present

in the copper layer and the sublayer near the silicon substrate, as shown in Figure 5 (a) and (g), which reveals the high atomic concentration of copper in the sublayer adjacent to the silicon substrate. The sublayer adjacent to the silicon substrate is copper silicide, according to the XRD spectra. XRD and STEM results show that copper silicide exists between the nickel silicide layer and a silicon substrate.

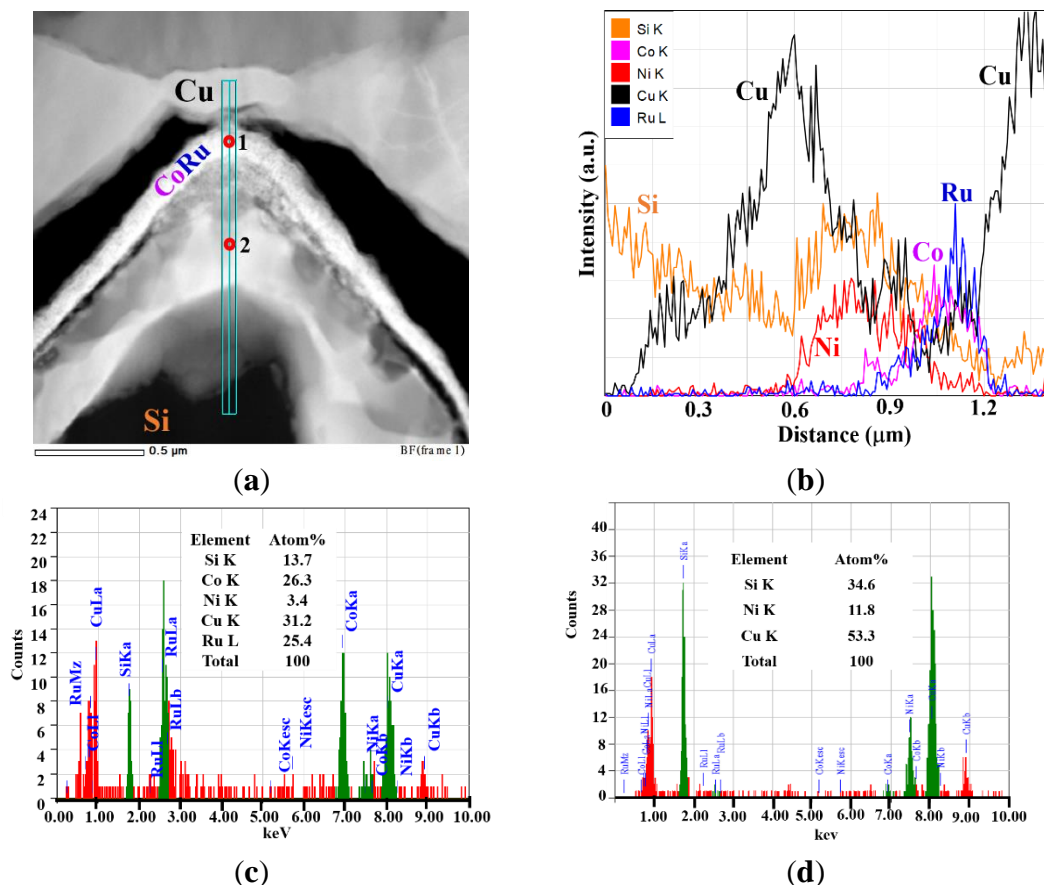


Figure 6. (a) STEM bright-field image of the sample annealed at 500 °C. (b) The composition analysis was carried out across the stack using STEM-EDS. The chemical compositions the red circles 1 (c) and 2 (d) shown in (a), respectively.

Figure 3 (a) shows four regions in the STEM image. The top and bottom regions are silicon substrate and electroplating copper layer from Figure 3 (f) and (b), respectively. The EDS elemental maps show nickel silicide and CoRu alloy layers between the copper film and silicon substrate from Figure 3 (c)-(g). The STEM-EDS spot elemental analysis shows that the ratio of Ru and Co is near 40 and 60. The composition of the CoRu alloy determined by STEM-EDS is in agreement with the SEM-EDS results. The thicknesses are approximately 90 nm and 240 nm for the CoRu alloy layer and nickel silicide layer, respectively, as shown in Figure 3 (a). The thicknesses of the CoRu alloy and nickel silicide layer estimated by the line scan (Figure 4) agree with the STEM micrograph (Fig. 3 (a)) and STEM-EDS maps (Fig. 3 (c)-(e) and (g)). The results indicate that the Cu/Co₆₀Ru₄₀/NiSi_x/Si structure was preserved after annealing at 300 °C. XRD analyses agree with the results of STEM.

The elemental copper map reveals that Cu is present in all layers, showing that Cu atoms diffused from the Cu film through the CoRu layer and nickel silicides into silicon, as shown in Figure 5 (b) and

(g). L. Stolt and F.M. D'Heurle reported that copper is the dominant diffusing species during the formation of Cu_3Si by the thermal reaction of copper on silicon at a temperature of $200\text{ }^\circ\text{C}$ [24]. Therefore, copper atoms can pass through the CoRu layer, and the nickel silicide layer moves readily to the silicon substrate and reacts to form Cu_3Si at $500\text{ }^\circ\text{C}$. The formation of the gap between the copper layer and CoRu layer indicated that the copper diffused into a silicon substrate and left void near the top CoRu layer. The copper in the CoRu layer was much less than that in the silicon substrate (Figure 6(b)), according to the weak Cu signal in the CoRu layer, which reveals that a small amount of copper atoms dissolved in the CoRu layer. The Ru layer also overlaps with the Co layer, as shown in Figure 5 (c) and (d). However, the distribution of cobalt is different from that of ruthenium. Part of the cobalt layer overlaps with part of the nickel layer, as shown in Figure 5 (d) and (e), which reveals that some cobalt has diffused into the nickel silicide layer and may have formed a cobalt silicide and nickel silicide [25, 26].

Fig. 6 (b) also shows that the intensities of ruthenium and cobalt in $\text{Cu}/\text{Co}_{60}\text{Ru}_{40}/\text{NiSi}_x/\text{Si}$ were almost the same. The results of the spot analysis reveal Co and Ru with an atomic ratio of $\sim 5:5$. We can also observe that the position of the most energetic intensity of ruthenium is different from the cobalt signal. The highest strength of the cobalt signal is located to the left of the ruthenium signal. This also reveals that some cobalt has diffused into the nickel silicide layer. Co and Ru have atomic ratios of $\sim 6:4$ and $\sim 5:5$ after annealing at 300 and $500\text{ }^\circ\text{C}$, respectively. The difference in atomic ratio Co and Ru between the sample annealed at 300 and $500\text{ }^\circ\text{C}$ is due to the dissolution of Co into the underlying nickel silicide.

The cobalt thin films on the surface polished (001) silicon via the vacuum plating process were heated, and cobalt silicides were formed. The phase of the cobalt silicide depended on the temperature of formation. The Co_2Si and CoSi formed at approximately $300\text{ }^\circ\text{C}$. The monosilicide CoSi was the only phase at approximately $400\text{ }^\circ\text{C}$. The CoSi and CoSi_2 were found at $500\text{ }^\circ\text{C}$. Only CoSi_2 existed at $600\text{--}900\text{ }^\circ\text{C}$ [25]. M. Garcia-Mendez et al. thermally treated the Co–Ni/p-Si/Si(100) system [26]. They found that the formation of Ni_2Si at approximately 523 K could occur. The formation of NiSi and Co_2Si could initiate at approximately 623 K . CoSi formed at 773 K [26]. Therefore, cobalt could diffuse into the nickel silicide layer and form a cobalt silicide and nickel silicide in the $\text{Cu}/\text{Co}_{60}\text{Ru}_{40}/\text{NiSi}_x/\text{Si}$ sample after annealing at $500\text{ }^\circ\text{C}$. STEM-EDS results show that cobalt atoms diffuse more easily to nickel silicide than ruthenium atoms at high temperatures.

The results of STEM-EDS and XRD analyses show that copper diffuses through the CoRu alloy layer and nickel silicide layer to the silicon substrate and reacts with silicon to form a copper silicide. Tan et al. reported that the sheet resistance of a pure Ru (10 nm) film increased at temperatures above $550\text{ }^\circ\text{C}$, which was due to the formation of the high resistivity phase Ru_2Si_3 . They also found that Ru/Ta or Ru/TaN barrier layers have superior stability for single Ru coatings [27]. Riedel et al. demonstrated that the TiN barrier fails due to the formation of randomly distributed defects due to the growth of copper silicide [9]. Hecker et al. reported that the failure mechanism of Ta-N thin films is due to local barrier breaks initiating barrier failure [10]. Chen et al. studied Ru–Ta and Ru thin films ($\sim 15\text{ nm}$ in thickness) as a diffusion barrier for Cu metallization on SiO_2/Si and Si substrates. The Ru and Ru–Ta layers prevent the diffusion of Cu until after annealing at 500 and $700\text{ }^\circ\text{C}$, respectively. The failure of the Ru and Ru–Ta barrier layer is related to the distribution of Cu through the barrier layer to the substrate [15]. In our

study, the copper silicide formed, and the $\text{Co}_{60}\text{Ru}_{40}$ alloy layer was preserved after annealing at 500 °C for 10 min. STEM results demonstrated that the failure mechanism of the $\text{Co}_{60}\text{Ru}_{40}$ barrier was different from the reports by Tan, Riedel, and Hecker [9,10,27]. The failure of $\text{Cu}/\text{Co}_{60}\text{Ru}_{40}/\text{NiSi}_x/\text{Si}$ can be attributed to copper penetration through the $\text{Co}_{60}\text{Ru}_{40}$ and nickel silicide layers, as confirmed by the XRD and STEM results and other literature [15].

4. CONCLUSIONS

This paper focuses on the failure behavior of the electroplated cobalt-ruthenium diffusion barrier for copper metallization. $\text{Cu}/\text{Co}_{60}\text{Ru}_{40}/\text{NiSi}_x/\text{Si}$ structure was preserved after annealing at 300 °C. The $\text{Co}_{60}\text{Ru}_{40}$ alloy layer below the copper layer seemed to remain after annealing at 500 °C for 10 min. However, there was a large gap between the $\text{Co}_{60}\text{Ru}_{40}$ and Cu layers. The formation of a hole indicates that the copper diffused into a silicon substrate and left void near the top $\text{Co}_{60}\text{Ru}_{40}$ layer. The electroplated $\text{Co}_{60}\text{Ru}_{40}$ alloy layer with a thickness of 90 nm was found to be a sound diffusion barrier against Cu up to 400 °C. According to the XRD and STEM analyses, the failure of $\text{Cu}/\text{Co}_{60}\text{Ru}_{40}/\text{NiSi}_x/\text{Si}$ can be attributed to copper penetration through the $\text{Co}_{60}\text{Ru}_{40}$ and nickel silicide layers and the formation of copper silicide.

References

1. Trube, J. International Technology Roadmap for Photovoltaics (ITRPV) Results from 2020, 12th ed., April 2021. <https://itrpv.vdma.org/download>.
2. D.H. Neuhaus and A. Munzer, *Adv. in Opt. Electron.*, 2007 24521.
3. Y. Tao, I. Yun, Ed. Rijeka: *InTech 2016, ch. 04*. [Online].
4. A.U. Rehman, S.H. Lee, *Materials*, 7 (2014) 1318-1341.
5. H. Rehman, S.H. Lee, E.G. Shin, and S.H. Lee, *Mater. Lett.*, 161 (2015) 181-184. <https://doi.org/10.1016/j.matlet.2015.08.063>
6. J. Bartsch, A. Mondon, K. Bayer, C. Schetter, M. Hörteis, and S.W. Glunz, *J. Electrochem. Soc.*, 157 (2010) H942-946.
7. A.A. Istratov and E.R. Weber, *Appl. Phys. A: Mater. Sci. Process.*, 66 (1998) 123-136.
8. S. Flynn and A. Lennon, *Sol. Energ. Mater. Sol. Cells*, 130 (2014) 309-316.
9. S. Riedel, S.E. Schulz, J. Baumann, M. Rennau, and T. Gessner, *Microelectron. Eng.*, 55 (2001) 213-218.
10. N. Fréty, F. Bernard, J. Nazon, J. Sarradin, and J.-C. Tedenac, *J. phase equilibria Diffus.*, 27 (2006) 590-597.
11. C.M. Liu, W.L. Liu, W.J. Chen, S.H. Hsieh, T.K. Tsai, L.C. Yang, *J. Electrochem. Soc.*, 2005, 152, G234-239.
12. R. Ecke, S. E. Schulz, M. Hecker, and T. Gessner, *Microelectron. Eng.*, 64 (2002) 261-268.
13. S. Wang, S. Suthar, C. Hoeflich, and B. J. Burrow, *J. Appl. Phys.*, 73 (1993) 2301.
14. C.W. Chen, J.S. Chen, and J.S. Jeng, *J. Electrochem. Soc.*, 155 (2008) H1003-1008.
15. J.S. Fang, J.H. Lin, B.Y. Chen and T.S. Chin, *J. Electrochem. Soc.*, 158 (2011) H97-102.
16. D.C. Perng, K.C. Hsu, S.W. Tsai and J.B. Yeh, *Microelectron. Eng.*, 87 (2010) 365-369.
17. M. Mühlbacher, G. Greczynski, B. Sartory, N. Schalk, J. Lu, I. Petrov, J.E. Greene, L. Hultman C. Mitterer, *Sci. Rep.*, 8 (2018) 5360.

18. Z. Li, Y. Tian, C. Teng, H. Cao, *Materials*, 13 (2020) 5049.
19. Q. Huang, K.B. Reuter, Y. Zhu, and VR Deline, *ECS J. Solid State Sci. Technol.*, 5 (2016) Q24-34.
20. Q. Huang, *ECS J. Solid State Sci. Technol.*, 5 (2016) P51-57.
21. Y.R. Cheng, W.J. Chen, K. Ohdaira, K. Higashimine, *Int. J. Electrochem. Sci.*, 13 (2018) 11516-11525.
22. R. Bernasconi and L. Magagnin, *J. Electrochem. Soc.*, 166 (2019) D3219-3225.
23. K.C. Wu, J.Y. Tseng, and W.J. Chen, *Appl. Surf. Sci.*, 516 (2020) 146139.
24. L. Stolt and F.M. D'Heurle, *Thin Solid Films*, 189 (1990) 269-274.
25. W. Lur and L.J. Chen, *J. Appl. Phys.*, 64 (1988) 3505-3511.
26. M. García-Méndez, F.F. Castellón, G.A. Hirata, M.H. Fariás, G. Beamson, *Appl. Surf. Sci.*, 161 (2000) 61-73.
27. J.J.Tan, X.P. Qu, Q. Xie, Y. Zhou, G.P. Ru, *Thin Solid Films*, 504 (2006) 231.

© 2021 The Authors. Published by ESG (www.electrochemsci.org). This article is an open access article distributed under the terms and conditions of the Creative Commons Attribution license (<http://creativecommons.org/licenses/by/4.0/>).